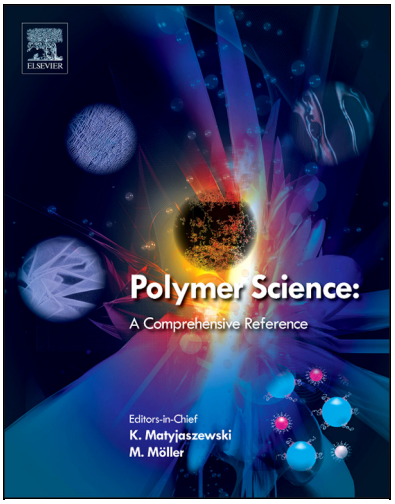

Dostálek J and Knoll W (2012) Plasmonics. In: Matyjaszewski K and Möller M (eds.) *Polymer Science: A Comprehensive Reference*, Vol 2, pp. 647–659. Amsterdam: Elsevier BV.

2.26 Plasmonics

J Dostálek and W Knoll, AIT-Austrian Institute of Technology GmbH, Vienna, Austria

2.26.1 Introduction

Various optical techniques were developed and applied for the observation of structural and dynamic characteristics of thin polymer films attached to a solid substrate including ellipsometry, attenuated total internal reflection Fourier transform spectroscopy (ATR-FTIR),[1] fluorescence spectroscopy,[2] spectroscopy of guided waves,[3] dynamic light scattering,[4] and fluorescence correlation spectroscopy.[5] Among these, the investigation of polymers tethered to a surface by spectroscopy of guided waves and by surface plasmon resonance (SPR)[6] offers the advantage of a nondestructive method that enables real-time and *in situ* monitoring of formation of polymer films, their swelling, and interaction with biomolecules. In particular, SPR-based methods found numerous applications for the investigation of nonfouling properties of polymer coatings[7] and protein immobilization and affinity interactions in polymer matrices[8,9] that are of interest in important fields such as biosensors,[10] antibacterial coatings,[11] cell adhesive surfaces,[12,13] and drug delivery.[14]

This chapter focuses on the characterization of polymer films by the spectroscopy of (leaky) surface plasmon (SP) and dielectric waveguide modes. The fundamentals of optics that are essential for the understanding and implementation of these techniques are presented (Section 2.26.2). Models that can be employed for the evaluation of optical response in order to assess the information on phenomena including adhesion of polymers on a surface, swelling of polymer films in solvents, and diffusion and interaction of biomolecules in polymers are discussed (Section 2.26.3). The performance characteristics of presented methods are illustrated with a focus on highly swollen polymer networks (cross-linked hydrogels and brushes) tethered on gold surfaces (Section 2.26.4).

2.26.2 Fundamentals of Guided Wave Optics

SP and dielectric waveguide modes represent a form of a propagation of electromagnetic radiation that is confined at a metal surface (SPs) or in a dielectric slab with higher refractive index than that of the surrounding medium (dielectric waveguide). At wavelengths λ in the visible and near infrared part of the spectrum, these waves are ideally suited for probing interfacial architectures with the thickness ranging from tens of nanometers to several micrometers. Furthermore, the key characteristics of these guided waves and schemes for their optical excitation and interrogation are introduced.

2.26.2.1 SP and Dielectric Waveguide Waves

SPs are optical waves that originate from coupled collective oscillations of the electron plasma and the associated electromagnetic field on metallic surfaces[15]. SPs propagate along a planar interface between a semi-infinite metal and a dielectric with the (complex) propagation constant β:

$$\beta = k_0 \sqrt{\frac{n_m^2 n_d^2}{n_m^2 + n_d^2}} \qquad [1]$$

where $k_0 = 2\pi/\lambda$ is wavenumber of light in vacuum, n_d is the refractive index of the dielectric, and n_m is the (complex) refractive index of the metal. SPs can be excited on a metallic surface at wavelengths below the metal plasma frequency ω_p. In the visible and near infrared part of the spectrum, mostly noble metals such as gold or silver are used for the excitation of SPs. The electromagnetic field of SP is transversally magnetically (TM) polarized, with the magnetic intensity vector parallel to the surface. As illustrated in **Figure 1(a)**, it evanescently decays into both metal and dielectric media. The majority of SP field is

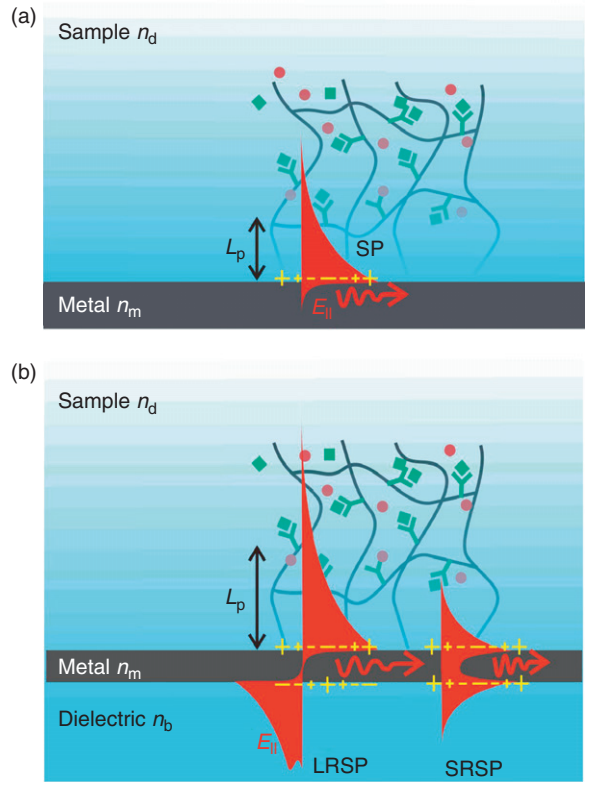

Figure 1 (a) SP propagating along a metal–dielectric interface; (b) LRSP and SRSP modes supported by a thin metallic film.

carried in a dielectric and only its small portion propagates in a metal. The field profile of SPs can be described by its penetration depth L_p that is defined as a distance from the surface at which the field magnitude drops to $1/e$. For example, at a boundary between gold and water with refractive indices $n_m = 0.1 + 3.5i$ and $n_d = 1.33$, respectively, the SP penetration depth into the dielectric reaches $L_p^d = 180$ nm and into the metal $L_p^m = 27$ nm at the wavelength $\lambda = 633$ nm.

Another type of SP waves can be observed on a thin metal film sandwiched between two dielectrics with identical refractive indices n_d (see **Figure 1(b)**). For a thickness of the metallic film d_m that is much larger than L_p^m, SPs propagate at each metal interface with the propagation constant β that was already described by eqn [1]. However, for smaller thicknesses of the metal film that are comparable to the SP penetration depth into the metal $d_m \sim L_p^m$, SP waves couple through the metallic film that gives rise to two new modes with symmetrical and antisymmetrical profile of electric intensity field. These modes are referred to as long-range surface plasmon (LRSP) and short-range surface plasmon (SRSP).[16] The propagation constants β of LRSP and SRSP modes can be determined by solving the following dispersion relation that has two unique solutions corresponding to each of these modes:

$$\tan(\kappa d_m) = \frac{2\gamma_d n_m^2/\kappa n_d^2}{1-(\gamma_d n_m^2/\kappa n_d^2)^2} \qquad [2]$$

where $\kappa^2 = (k_0^2 n_m^2 - \beta^2)$ and $\gamma^2_d = \beta^2 - k_0^2 n^2_d$. The real part of the propagation constant $\mathrm{Re}\{\beta\}$ of SRSP mode is larger than that of regular SPs and $\mathrm{Re}\{\beta\}$ of LRSPs is lower than that of regular SPs. The reason is that SRSP mode is strongly confined (guided) by the metal film. Opposite to that, the LRSP is guided weakly by the metallic film. The imaginary of the propagation constant $\mathrm{Im}\{\beta\}$ defines the damping of SP modes that occurs due to the (Ohmic) losses in the metal. SRSP mode exhibits higher $\mathrm{Im}\{\beta\}$ that associates with increased losses. LRSP mode can propagate over longer distances and thus exhibits lower $\mathrm{Im}\{\beta\}$. By changing the metal thickness d_m (typically few tens of nanometers) and through introducing a small perturbation to the symmetry (refractive index of a dielectric above and below the metal film is slightly different), the penetration depth L_p^d of LRSPs can be tuned to reach up to several micrometers.[17] In addition, more complex layer structures can be used in order to tailor the characteristics of LRSPs for specific needs. Two parallel metallic films separated by a buffer dielectric layer with identical refractive index as one of the surrounding dielectrics n_d support two coupled LRSP modes. For instance, a polymer film that is highly swollen in water can be probed with penetration depths of $L_p^d = 364$ and 950 nm by using a structure consisting of two gold films with a thickness of $d_m = 22.5$ nm and a buffer layer thickness of 640 nm with refractive index 1.337.[18]

A thin polymer film that is attached to a metal surface can support guided waves if its refractive index and the thickness are sufficiently large (see **Figure 2**). These waves are confined in a polymer film through the reflecting metal surface and by total internal reflection at the interface with lower refractive index dielectric. Let us note that only discrete modes can propagate through the film for which the field reflected from the metal and dielectric interfaces constructively interferes. This type of waveguide can support guided waves for both transverse magnetic (TM) and transverse electric (TE) polarization (for TE polarization, the electric intensity vector is parallel to the surface). The propagation constants β of TM-polarized waves propagating in polymer film can be determined by solving the following dispersion relation:

$$\tan(\kappa d_h) = \frac{\frac{\gamma_d n_h^2}{\kappa n_d^2} + \frac{\gamma_m n_h^2}{\kappa n_m^2}}{1-\left(\frac{\gamma_d n_h^2}{\kappa n_d^2}\right)\left(\frac{\gamma_m n_h^2}{\kappa n_m^2}\right)} \qquad [3]$$

where n_h and d_h are refractive index and thickness of the polymer film, respectively. The terms $\kappa^2 = (k_0^2 n_h^2 - \beta^2)$, $\gamma^2_m = \beta^2 - k_0^2 n^2_m$, and $\gamma^2_d = \beta^2 - k_0^2 n^2_d$ are the transverse propagation constants in the polymer film, the metal, and the liquid, respectively. For TE polarization, the dispersion relation yields:

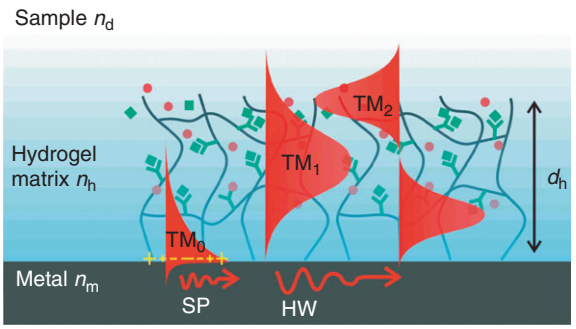

Figure 2 Hydrogel film attached to a metallic surface supporting guided waves.

$$\tan(\kappa d_h) = \frac{\frac{\gamma_d}{\kappa} + \frac{\gamma_m}{\kappa}}{1 - \left(\frac{\gamma_d}{\kappa}\right)\left(\frac{\gamma_m}{\kappa}\right)} \quad [4]$$

In general, the number of guided waves in a polymer slab increases with its thickness d_h and refractive index n_h. The real part of the propagation constant of these modes is lower than the momentum of light in a bulk dielectric with the same refractive index as that of the slab $\mathrm{Re}\{\beta\} < k_0 n_d$.

2.26.2.2 Coupling of Light to SP and Dielectric Waveguide Waves

In order to probe a polymer film with SP or polymer waveguide modes, attenuated total reflection (ATR) method with Kretschmann configuration can be used (see Figure 3). In this popular method, a light beam is launched to a prism with a high refractive index n_p and is reflected from its base under an angle of incidence θ that is higher than the critical angle $\theta > \sin^{-1}(n_d/n_p)$. On the prism base, layer architecture with a thin metal film supporting SP and/or polymer-guided waves is attached. The coupling between the light beam in the prism and a guided wave propagating at the prism base occurs via their evanescent fields at distinct angles of incidence θ that fulfill the following phase-matching condition:

$$k_0 n_p \sin(\theta) = \mathrm{Re}\{\beta\} \quad [5]$$

The resonant interaction between a monochromatic light beam and guided waves on the sensor surface is manifested as a series of resonant dips in the angular reflectivity spectrum $R(\theta)$ located at angles for which the condition (eqn [5]) holds (see Figure 4(a)). Upon the coupling to guided waves, the energy of incident light beam is transferred to guided waves propagating along the sensor surface leading to a decreased reflectivity. The coupling angles are sensitive to refractive index variations in the top dielectric δn_d that alter the propagation constant β of guided waves (see eqns [1]–[4]) and subsequently change the coupling condition (eqn [5]). The coupling strength to SP-guided waves can be controlled by the thickness of metallic or low-refractive index dielectric buffer layers.

For the sake of illustration, Figure 4(b) shows the characteristic profile of LRSP and hydrogel polymer waveguide (HW) modes. In these simulations, a structure consisting of a low-refractive index fluoropolymer layer (refractive index $n_b = 1.337$ and thickness $d_b = 715$ nm), gold film (thickness $d_m = 13.2$ nm and refractive index $n_m = 0.269 + 2.58i$), hydrogel layer (thickness $d_h = 1800$ nm and refractive index $n_h = 1.345$), aqueous sample (refractive index $n_d = 1.333$), and a wavelength of $\lambda = 633$ nm was assumed. This figure reveals that the LRSP and HW exhibit different profiles of field. The intensity of LRSP peaks at the gold surface and it exponentially decays through the hydrogel film with the penetration depth of around $L_p = 920$ nm. The HW field intensity reaches its maximum in the vicinity of the outer hydrogel interface and it evanescently decays into the aqueous sample with larger penetration depth than LRSPs.

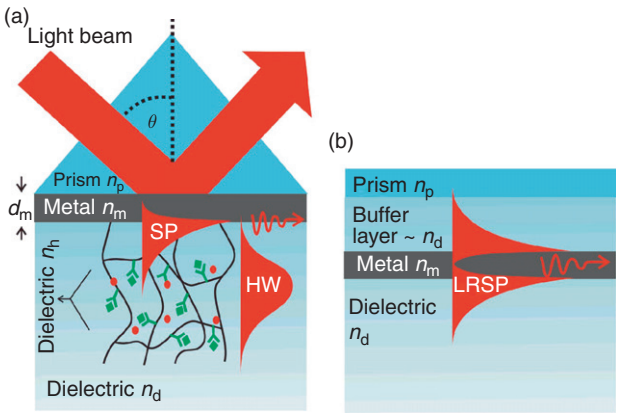

Figure 3 (a) ATR method with Kretschmann geometry for the excitation of SP and polymer waveguide modes; (b) layer architecture for the excitation of LRSP modes.

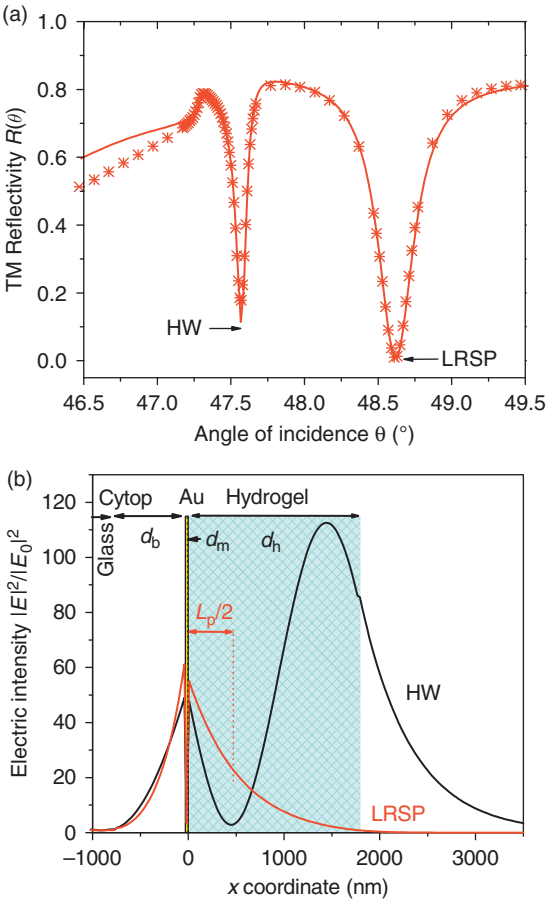

Figure 4 (a) Angular reflectivity spectrum and (b) electric intensity field profile upon the resonant coupling to LRSP and HW waves.

2.26.2.3 Implementation of Spectroscopy of SP and Polymer Waveguide Waves

A typical implementation of ATR optical setup for angular spectroscopy of SPs is depicted in Figure 5. It consists of a laser emitting a collimated monochromatic beam that passes through a polarizer for selecting its TM or TE polarization. Afterward, the intensity of polarized light beam is modulated by a chopper and it is launched into a prism coupler. The prism coupler is mounted on a rotation stage in order to control the angle of incidence θ at which the light beam hits a sensor chip that is optically matched on the prism base by using a refractive

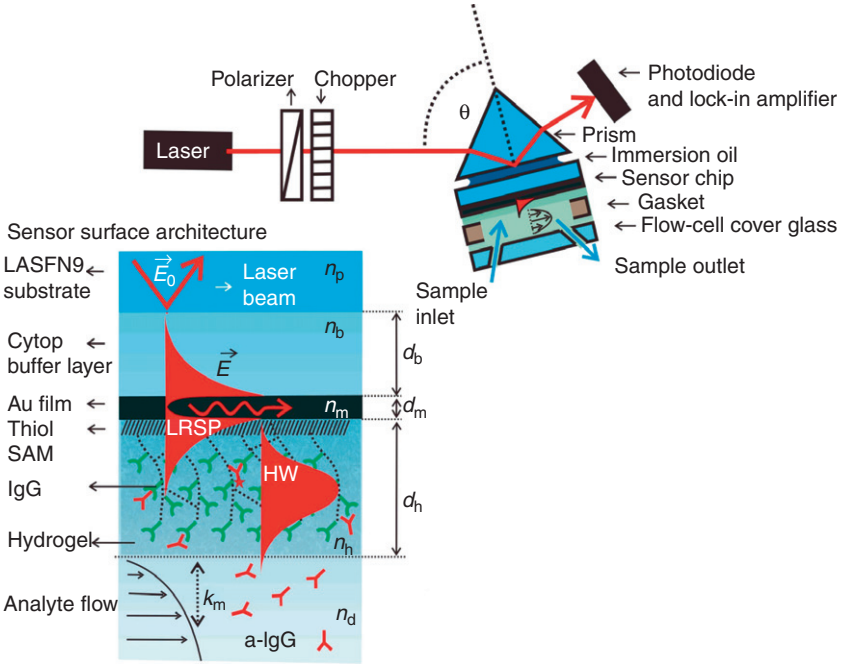

Figure 5 Implementation of ATR method with Kretschmann configuration for the excitation of LRSP and HW waves.

index matching oil. To the sensor chip surface, a flow cell is attached in order to flow (liquid or gas) samples. The reflected light is projected at a photodiode that is connected to a lock-in amplifier. The lock-in amplifier allows the detection of the intensity of reflected light beam at the chopped frequency and thus the filtering out of a background signal. This simple configuration of SPR spectrometer can be employed for the measurement of the angular reflectivity spectrum $R(\theta)$ and its changes in time. Refractive index changes associated with investigated effects in thin polymer films attached to the sensor chip surface can be observed from variations in the reflectivity spectrum $R(\theta)$, particularly, as a shift in the resonance dips. Typically, refractive index changes on the surface as small as 10^{-6} can be measured with the subsecond time resolution.

The sensor chip consists of a glass slide with SPR active layers deposited on its top. For the excitation of SPs, gold is a popular material due to its stability and range of surface chemistries available based on, for example, thiol self-assembled monolayers (SAMs) that allow the control of the surface properties (e.g., thiols with hydrophilic polyethylene glycol moieties or hydrophobic methyl groups) and provide linkers for coupling of other molecules (e.g., thiols with carboxylic, biotin, or bezophenon groups). Preferably, gold films with the thickness of $d_m \sim 50$ nm are used which provide the highest coupling efficiency (the reflectivity minimum at the resonant angle approaches zero). Metallic films such as gold can be prepared by vacuum thermal evaporation or sputtering. A thin chromium or titanium layer can be deposited between the gold and the glass in order to promote the adhesion and prevent delaminating of gold film. For the excitation of LRSPs, a buffer layer needs to be deposited between the substrate and the gold film in order to achieve a refractive index symmetrical structure. This buffer layer has to exhibit the refractive index n_b close to that of water n_d or investigated polymers n_h. Different commercially available Teflon-based materials[19,20] (Teflon AF from Dupont Inc., USA, with $n_b = 1.31$ and Cytop from Asahi Inc., Japan, with $n_b = 1.34$), low-refractive index dielectrics such as aluminum fluoride (AlF_3, $n_b = 1.34$)[21] or magnesium fluoride (MgF_2, $n_b = 1.38$)[20] and nanoporous silicates (the refractive index can be tuned by the size of pores) were used as a buffer layer with a refractive index close to that of water. These materials can be spin coated (Teflon) or deposited by vacuum thermal evaporation or sputtering (magnesium and aluminum fluoride). As shown in literature,[17] gold films with thicknesses $d_m < 20$ nm exhibit an island morphology on surfaces with low surface energy such as Teflon. Such gold films exhibit increased roughness and their optical properties are deteriorated compared to structures with smooth gold surfaces. The roughness and optical properties can be improved by increasing the surface energy by, for example, plasma etching.[22]

Let us note that various advanced optical setups for the spectroscopy of SPs were developed in order to reach higher sensitivity, wider dynamic range, and parallel observation of multiple interactions.[23] In addition, SPR spectrometers can be combined with other techniques including quartz crystal microbalance (QCM),[24] electrochemistry (EC),[25] and fluorescence spectroscopy (SP-enhanced fluorescence spectroscopy (SPFS)).[26]

2.26.3 Observation of Thin Polymer Films

2.26.3.1 Refractive Index Profile

The reflectivity spectrum $R(\theta)$ measured upon the coupling to guided waves propagating in a polymer film carries information on its refractive index profile. This profile can be obtained by the analysis of $R(\theta)$ and its changes can be tracked in real time. By using certain parameterization, the dependence of the refractive index of the polymer film on the distance perpendicular to the surface $n(x)$ can be obtained by fitting $R(\theta)$ with a Fresnel reflectivity-based model (see **Figure 4(a)**). In order to

simulate the reflectivity spectrum from a multilayer system, numerous algorithms based on transfer matrix formalism[28] were developed. In general, more detailed profiles of the refractive index $n(x)$ can be assessed (i.e., more exact parameterization can be used) with an increasing number of probing surface waves that exhibit different profiles of electromagnetic field. This feature is an important difference compared to regular SPR that probes the sensor surface with (only one) SP mode. Regular SPR thus allows only the measurement of optical thickness $(n_h - n_d)d_h$ (for films with the thickness $d_h \ll L_p^d$) or refractive index of the film n_h (for films with the thickness $d_h > L_p^d$) and cannot independently decouple the information on the refractive index n_h and thickness d_h.

The probing with two SP modes exhibiting different profiles of electromagnetic field allows an independent determination of the refractive index n_h and thickness d_h of polymer films that do not support multiple waveguide modes (typically for thicknesses $d_h < 1\ \mu m$). For instance, this approach was implemented by using a sensor chip that supported coupled LRSP modes[18] or by combined spectroscopy SP and polymer-guided waves.[29] For the probing by two different modes, the polymer refractive index profile can be described by two parameters – thickness d_m and refractive index n_h. In this approximation referred to as a 'box model', the dependence of the refractive index perpendicular to the surface $n(x)$ is assumed to be the following function:

$$n(x) = n_d + (n_h - n_d)H(d_h - x) \quad [6]$$

where x is the axis perpendicular to the sensor surface ($x = 0$ is the position at the interface between the metal and the polymer) and H is the Heaviside step function. An example of a reflectivity spectrum $R(\theta)$ that was fitted by using a box model is shown in Figure 4(**b**).

For polymer films with higher thickness (typically >1 μm), the probing by multiple HW modes allows the determination of a more detailed profile of the refractive index $n(x)$ perpendicular to the surface (see Figure 6). Similarly to the approaches used for the investigation of planar waveguides, reversed Wenzel–Kramers–Brillouin (WKB) approximation can be employed for the reconstruction of the spatial dependence of refractive index $n(x)$ perpendicular to the surface if it does not change rapidly over the wavelength distances.[30] Compared to direct fitting of a refractive index profile, this method allows the determination of the refractive index profile in a simpler manner and it is less demanding in terms of computation power. In general, various parameterizations can be used including a piecewise function[27] or the following smooth function that takes into account the polymer film density gradient at its outer interface:[30]

$$n(x) = n_d + \frac{n_h - n_d}{\gamma}\left[1 - (1-\gamma)^{erfc\left(\frac{x}{d_h}\right)}\right] \quad [7]$$

where d_h and n_h are the effective thickness and refractive index, respectively, and γ is the thickness of the top polymer region in which the density gradually decreases toward the solvent medium with the refractive index n_d.

Simultaneous spectroscopy of guided waves in TM and TE polarization can be employed for the measurement of birefringence (refractive indices n_h 'seen' by electromagnetic waves with electric intensity vector parallel and perpendicular to the film are different) that is associated with anisotropy of a polymer film. From the difference between the refractive index determined through the probing by TE-polarized waves (electric intensity vector parallel to the surface) and TM-polarized waves (electric intensity vector with a component perpendicular to the surface), information on phenomena such as lateral stress[31] or orientation of polymer chains[32] can be deduced.

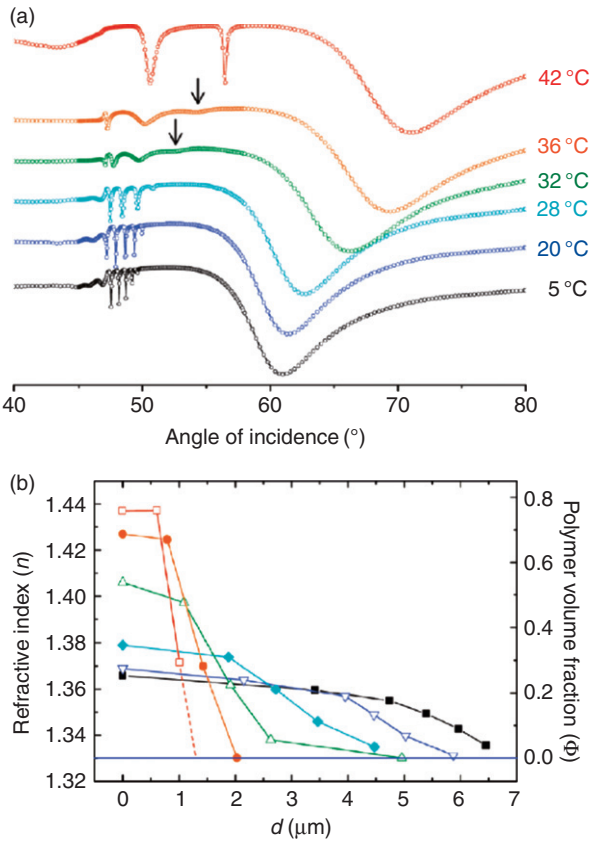

Figure 6 (a) Series of reflectivity spectra measured for thin responsive PNIPAAM hydrogel film tethered to a gold surface with different swelling ratio controlled by a temperature of a liquid flowed over the surface and (b) determined refractive index profile. Reprinted with permission from Junk, M. J. N.; Anac, I.; Menges, B.; Jonas, U. *Langmuir* **2010**, *16*, 12253–12259.[27] Copyright 2010 American Chemical Society.

2.26.3.2 Density and Structure of Polymer Films

The refractive index of polymer films can be related to the polymer density by using effective medium theories such as Maxwell–Garnet or Bruggemann theory[33,34] that in the limit of small polymer volume content give identical results. These theories can be applied for random mixtures of a polymer and a solvent where the size of grains (or pore size) is much smaller than the wavelength λ. The polymer volume content in a swollen polymer (hydrogel) can be calculated from the optical properties of a film as

$$f = \frac{(n_{h_2} - n_{d_2})(n_{n-dry_2} + 2n_{d_2})}{(n_{h_2} + 2n_{d_2})(n_{n-dry_2} - n_{d_2})} \quad [8]$$

where n_{h-dry} and n_h are the refractive indices of a dry and swollen polymer film, respectively. Let us note that the swelling

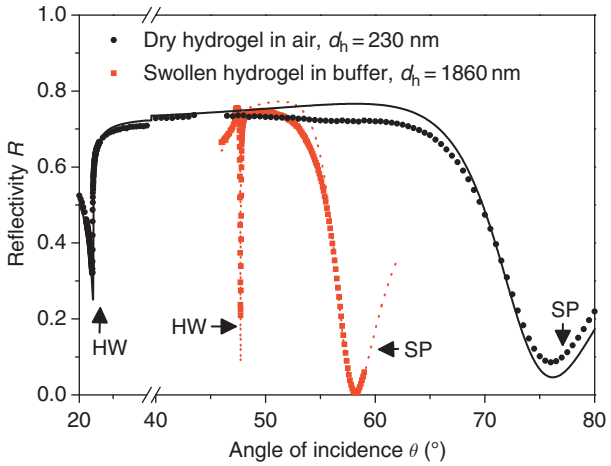

Figure 7 Spectroscopy of SP and HW waves propagating in a thin PNIPAAM-based film on a 50 nm gold film in contact with air and a buffer.

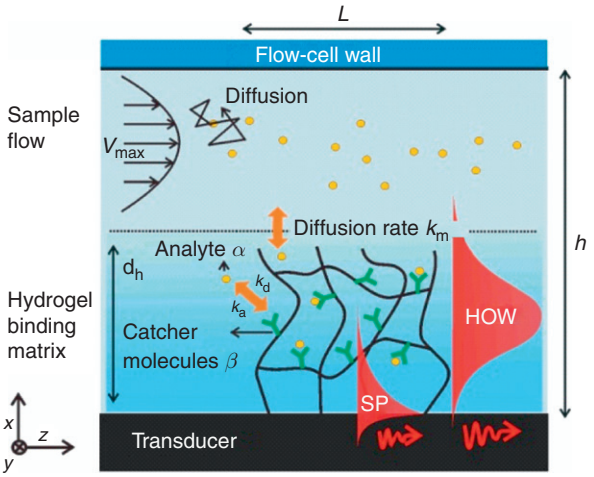

Figure 8 The scheme of a flow-cell channel with analyte diffusing from a sample to a hydrogel binding matrix attached to its bottom.

ratio of a hydrogel film is defined from its thicknesses in swollen state d_h and dry state d_{h-dry} as $SR = d_h/d_{h-dry}$ and it is inversely proportional to the polymer volume content $SR = 1/f$. Based on the Lorenz–Lorenz relation,[33] the surface mass density of the gel Γ can be approximated for small refractive index difference contrast $n_h \sim n_d$ as

$$\Gamma = (n_h - n_d) d_h \frac{\partial c}{\partial n_h} \quad [9]$$

where the coefficient $\partial n_h/\partial c \sim 0.2\ mm^3\ mg^{-1}$ relates changes in the refractive index and concentration of typical organic materials such as polymers or proteins.[35]

Figure 7 shows angular reflectivity spectra $R(\theta)$ that were measured for a thin poly(*N*-isopropylacrylamide) (PNIPAAM)-based hydrogel film in contact with air and after its swelling in phosphate-buffered saline (PBS).[36] By fitting the two distinct resonances at $\theta_{HW} = 21.9°$ and $\theta_{SP} = 76°$ that are associated with the excitation of hydrogel polymer waveguide (HW) and SP modes in a dry polymer layer, its thickness $d_{h-dry} = 230$ nm and refractive index $n_{h-dry} = 1.48$ was determined. After swelling in a solvent (PBS), the HW and SP coupling angles shifted to $\theta_{HW} = 47.75°$ and $\theta_{SP} = 58.20°$, respectively. The analysis of corresponding reflectivity spectrum revealed that the thickness of the swollen gel increased to $d_h = 1.86$ μm and the refractive index decreased to $n_h = 1.3454$. This refractive index is close to that of PBS $n_d = 1.3340$ and it corresponds to the polymer volume fraction of $f = 8\%$. This value is in agreement with the swelling ratio SR determined from the thicknesses d_h and d_{h-dry}.

2.26.3.3 Diffusion and Interaction of Molecules in Polymer Films

The probing with SP modes enables the observation of diffusion and binding of molecules in polymer films that are associated with changes in the refractive index n_h. Further, let us assume molecules dissolved in a liquid that is flowing through a flow channel over a solid sensor surface with tethered polymer. As shown in Figure 8, the flow velocity of a liquid sample is zero at the surface (due to the nonzero liquid viscosity). For a laminar flow, the flow velocity is parallel to the surface and its magnitude exhibits a parabolic profile across a flow channel. For a surface coated with a polymer that swells in the liquid (hydrogel), the liquid flow penetrates in the gel only to a very small distance that is comparable to the gel mesh size.[37] Therefore, the transport of analyte molecules from a sample to the hydrogel binding matrix is dominantly driven by diffusion.

The two-compartment model was developed to describe reactions on a surface affected by a diffusion mass transfer of an analyte from a solution to the surface.[38] In this model, the zero flow velocity at the surface is taken into account through a (hypothetical) unstirred layer with the thickness depending on a volumetric sample flow rate v and the geometry of the flow channel (i.e., on its depth h, length L, and width w). Diffusion rate k_m of analyte molecules through the unstirred layer to and from the surface can be expressed as

$$k_m = 1.378 \left(\frac{v_{max} D_s^2}{hL} \right)^{1/3} \quad [10]$$

where D_s is the analyte diffusion coefficient in the bulk solution (sample) and $v_{max} = 3v/(2hw)$ is the flow velocity in the center of the flow cell. For example, immunoglobulin G (IgG, molecular weight around 150 kDa) diffuses in an aqueous environment with the diffusion coefficient $D_s = 3 \times 10^{-5}\ mm^2\ s^{-1}$.[39] For a typical flow channel with the depth $h = 100$ μm, length of $L = 10$ mm, width of $w = 5$ mm, and the flow velocity of $v_{max} = 5\ mm\ s^{-1}$, the analyte molecules diffuse to the sensor surface with the rate $k_m \sim 10^{-3}\ mm\ s^{-1}$.

Further, we introduce a numerical model that describes diffusion mass transport and binding of molecules to affinity partners immobilized in a hydrogel film. This model was applied for the investigation of large-binding capacity hydrogel matrices[29] and it is based on a theory developed by Schuck *et al.*[40] for the evaluation of affinity binding constants by using SPR biosensor technology with a thin dextran brush binding matrix.[38,41] In the model, we assume a reaction between analyte molecules A that are dissolved in a sample (at a concentration α_0) and catcher molecules B that are immobilized in a hydrogel (with a concentration β). For simplicity, the reaction fulfills the following conditions: (1) all analyte and

catcher molecules are identical and one catcher molecule can bind only one analyte molecule, (2) analyte molecules react only with catcher molecules, and (3) each individual binding event is independent of the occupancy of other catcher molecules. The dynamic equilibrium of the reaction between α and β is given as

$$A + B \underset{k_d}{\overset{k_a}{\rightleftarrows}} AB \qquad [11]$$

where k_a and k_d are the association and dissociation rate constants, respectively.

For a flow channel geometry depicted in Figure 8, Cartesian coordinates with the x-axis perpendicular to the surface and the z-axis parallel to the sample flow are used. Laminar flow of a sample through the flow cell is assumed. This condition holds for the flow conditions with Reynolds number Re < 2100 (let us note that the Reynolds number is equal to $\mathrm{Re} = (v/h) \cdot 0.998\ \mathrm{mm^2\,s^{-1}}$ for water at 20 °C). In addition, the dependence of the concentration of free α and captured γ analytes on y- and z-axes (parallel to the sensor surface) is neglected. This approximation is valid for geometries in which Peclét number $\mathrm{Pe} = v_{max}h^2/(D_sL)$ is large ($\mathrm{Pe} \gg 1$). Under these conditions, the time and spatial dependence of the concentration of captured analyte $\gamma(x,t)$ can be determined by solving the following set of partial differential equations (PDEs):

$$\frac{\partial \alpha}{\partial t} = D_g \frac{\partial^2 \alpha}{\partial x^2} - \frac{\partial \gamma}{\partial t} \qquad [12]$$

$$\frac{\partial \gamma}{\partial t} = k_a \alpha(\beta - \gamma) - k_d \gamma \qquad [13]$$

The first equation [12] describes the diffusion of analyte α through the gel that is depleted due to the reaction with unoccupied catcher molecules. The second equation [13] describes the reaction between analyte molecules α and catcher molecules β that leads to forming a complex γ. In eqn [12], the coefficient D_g stands for the analyte diffusion coefficient in the gel.

Partial differential equations [12]–[13] can be solved for a defined set of boundary and initial conditions. For sample flow that starts at $t = 0$, the conditions ([14]–[18]) can be applied. Equations [14] and [15] define the zero concentration of free α and captured γ analytes, respectively, before introducing a sample to the flow cell. Equation [16] ensures that there are no sources of the analyte α in the gel at time $t = 0$, eqn [17] defines the analyte flux through the inner hydrogel interface (i.e., analyte cannot pass through the solid support on which gel is attached), and eqn [18] describes that the analyte flux through the outer interface (with the sample) is driven by the mass diffusion rate k_m.

$$\alpha(x, t = 0) = 0 \qquad [14]$$

$$\gamma(x, t = 0) = 0 \qquad [15]$$

$$\frac{\partial \alpha}{\partial x}(x, t = 0) = 0 \qquad [16]$$

$$\frac{\partial \alpha}{\partial x}(x = 0, t) = 0 \qquad [17]$$

$$\frac{\partial \alpha}{\partial x}(x = d_h, t) = \frac{k_m}{D_g}\left[\alpha_0 - \alpha(d_h, t)\right] \qquad [18]$$

The set of partial differential equations [12] and [13] with boundary and initial conditions ([14]–[18]) describe diffusion of analyte from a sample to the surface and *vice versa* (diffusion rate k_m), diffusion of analyte through the polymer network (diffusion coefficient D_g), and the affinity interaction with binding sites (affinity binding rates k_a and k_d). These equations do not have an analytical solution; however, they can be solved numerically by using, for example, the Crank–Nicholson method. An analytical solution can be found only for simplified cases such as (1) for the slow analyte diffusion through the gel without the affinity binding, and (2) for the affinity binding that is not hindered by the diffusion through the polymer.

For illustration, the spatial distribution of captured analyte in a hydrogel film $\gamma(x)$ that was calculated by using the numerical model is presented in Figure 9. It shows the distribution of captured analyte in a hydrogel film with the thickness varied between $d_h = 64$ and 1440 nm and diffusion rate was assumed to be equal to $k_m = 2 \times 10^{-3}\ \mathrm{mm\,s^{-1}}$. The hydrogel films carry catcher molecules that are assumed to be homogenously distributed through the film at the concentration $\beta = 0.9$ mM and reacted for 30 min with analyte molecules flowed over the surface at the concentration of $\alpha_0 = 0.67$ pM. For such a low analyte concentration, the binding in the gel is far from saturation $\gamma \ll \beta$. In such gel, the analyte molecules diffusing from a sample into the gel are captured within a characteristic time t_a and thus can diffuse only to a limited distance from the outer gel interface. The average diffusion time can be obtained from eqn [13] as $t_a = \ln(2)/(k_a\beta)$ that corresponds to the following diffusion depth d_p derived by using Fick's law:

$$d_p = \sqrt{\frac{4D_g \ln(2)}{k_a \beta}} \qquad [19]$$

For the discussed example investigated by Huang *et al.*, the diffusion penetration depth reaches $d_p = 380$ nm for the diffusion coefficient of $D_g = 3 \times 10^{-7}\ \mathrm{mm^2\,s^{-1}}$ and increases to $d_p = 1.2\ \mu\mathrm{m}$ for $D_g = 3 \times 10^{-6}\ \mathrm{mm^2\,s^{-1}}$ as seen in Figure 9. These data illustrate that a more homogenous distribution of $\gamma(x)$ is established in gel with small thickness d_h or for large diffusion coefficients D_g.

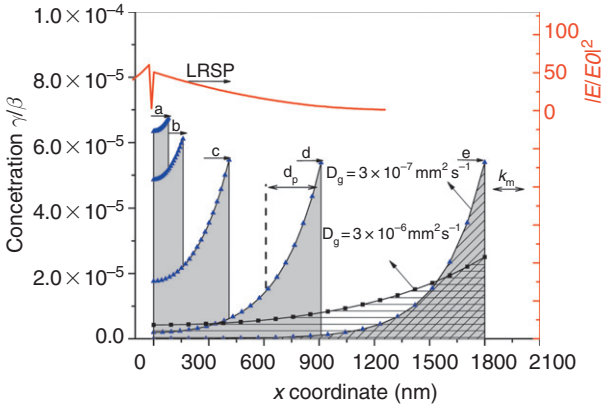

Figure 9 The comparison of simulated spatial distribution of captured analyte $\gamma(x)$ in a hydrogel film with the thickness of (a) $d_h = 64$ nm, (b) $d_h = 130$ nm, (c) $d_h = 330$ nm, (d) $d_h = 730$ nm, and (e) $d_h = 1440$ nm. Diffusion coefficient in the hydrogel of $D_g = 3 \times 10^{-6}\ \mathrm{mm^2\,s^{-1}}$ (black ■) and $D_g = 3 \times 10^{-7}\ \mathrm{mm^2\,s^{-1}}$ (blue ▲) is shown for the hydrogel thickness of $d = 1800$ nm.

2.26.4 Applications

This section describes applications of the spectroscopy of SP and polymer-guided waves for the observation of formation and swelling of polymer films, investigation of diffusion and interaction of molecules in polymer networks, and characterization of polymer nonfouling surfaces. Let us note that this section is not a complete review in these fields and only a limited set of examples were selected for the sake of illustration of the described methods, particularly, from the field of functional hydrogels for biosensor and smart surfaces development.

2.26.4.1 Formation of Polymer Films

SPR was employed for the observation of kinetics of adsorption and desorption of synthetic[42,43] and natural[44] polymers on gold surfaces with controlled surface characteristics (e.g., hydrophobic or hydrophilic). It allows time-resolved evaluation of formation of polymer films and provides leads on the structure and adsorption mechanism in different stages of the polymer film growth when combined with an appropriate model. For instance, Brandani *et al.*[42] studied adsorption of a triblock copolymer $PEO_nPPO_mPEO_n$ on hydrophobic surface for different copolymer architectures. They observed Langmuir-like adsorption kinetics in the initial stage of polymer film adsorption and studied the effect of unimer and micel copolymer forms on the amount of bound polymer. Let us note that range of theories describing adsorption and diffusion of molecules on surfaces can be found in literature.[45]

2.26.4.2 Swelling of Polymer Films

SPR combined with spectroscopy of polymer-guided waves was extensively employed for the observation of responsive hydrogel films.[30,46–48] *N*-Isopropylacrylamide (NIPAAM) is one of the prominent materials that was investigated in great detail and that found numerous applications in biomaterials, drug delivery, and actuators.[49] In water, it exhibits lower critical solution temperature (LCST) around 32 °C. An example of the observation of thin NIPAAM-responsive film by the spectroscopy of polymer-guided film is given in Figure 6.[27] The Figure 6(a) shows measured reflectivity spectra from a photo-cross-linked PNIPAAM-based hydrogel film that gradually changed its swelling upon varying the temperature between $T = 5$ and 52 °C. One can see that for high temperatures when the gel is collapsed, the reflectivity spectra exhibit two polymer waveguide resonances located at angles θ between 50° and 60°. For low temperatures, the gel is in a swollen state and five HW resonances located at angles that are below 50° are observed. The reason for the increased number of resonances and their shift to lower angles is a swelling of the gel that is associated with increased thickness d_h and decreased refractive index n_h. The refractive index profile $n(x)$ was determined by a using piecewise function through the analysis of the reflectivity spectra in Figure 6(a) as described in the Section 2.26.3.1. The results in Figure 6(b) show that the hydrogel in a collapsed state exhibited thickness of $\sim 1\,\mu m$. In a swollen state, the polymer chains stretched up to $\sim 6\,\mu m$ distance from the metallic film. Through the swollen gel, the polymer refractive index was continuously decreasing from the gold surface and the transition region exhibited the thickness γ of several micrometers.

Polymer films that are too thin to support guided waves can be investigated by multiple SP spectroscopy. For instance, the response to pH of NIPAAM-based hydrogel films with varied cross-linking density and thickness $d_h = 600–700\,nm$ was observed by the spectroscopy of coupled LRSPs.[18] The penetration depth of these modes was tuned in the range between 365 and 950 nm in order to match the thickness of investigated films. Moreover, investigating thinner polymer films is possible by simultaneous probing with multiple SP modes which at different wavelengths exhibit different profiles of electromagnetic field intensity. Refractive index n_h and thickness d_h of biopolymer films deposited by layer-by-layer method were measured by multiwavelength SP spectroscopy[50] and spectroscopy of Bragg-scattered SP modes.[51] In these methods, the penetration depth of SPs at the interface between gold and water L_p^d can be varied in the range 50–250 nm and allows the determination of both n_h and d_h for films with the thickness below 100 nm.

2.26.4.3 Diffusion and Binding of Biomolecules in Polymer Films

SP-based optics can be applied for the investigation of diffusion and interaction of molecules in polymer films. First, the diffusion coefficient of small aromatic hydrocarbons (benzene and toluene with molecular weights 78 and 92 Da, respectively) in a fluoropolymer film was measured by the spectroscopy of SP and polymer-guided waves in the late 1990s.[52] Compared to fluorescence-based techniques such as fluorescence correlation spectroscopy,[5] their approach does not require labeling of molecules with fluorophores and allows investigation of thinner polymer films. Podgorsek *et al.*[52] deposited 1–2 μm thick Teflon AF1600 layer on a 50 nm thick silver film and flowed benzene and toluene vapors through a flow cell interfaced with the polymer film. The refractive index changes in close vicinity to the inner interface between the polymer and the silver were measured in time by using SPR. As seen in Figure 10, after the injection of a gas with benzene vapors, the refractive index gradually increased and reached equilibrium after ~100 s. The measured SPR kinetics were fitted

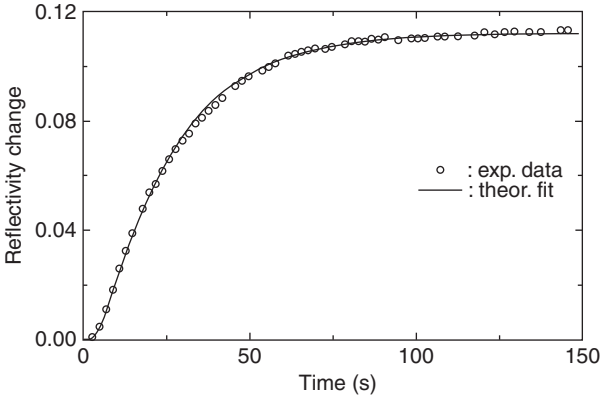

Figure 10 SPR sensor response kinetics measured upon the probing of the diffusion of benzene through a fluoropolymer polymer film. Experimental data are shown as circles and the fitted curve as a line. Reprinted with permission from Podgorsek, R. P.; Franke, H. *Appl. Phys. Lett.* **1998**, *73*, 2887–2889.[52] Copyright 1998 American Institute of Physics.

with a model (see Section 2.26.3.3) where the concentration of benzene at the outer polymer interface was assumed to be constant ($k_m \to \infty$) and the interaction of analyte with polymer was neglected ($\beta = 0$). As Figure 10 shows, this simplified model allowed for excellent fitting of the experimental data for the diffusion benzene coefficient of $D_g = 4.9 \times 10^{-8}\,mm^2\,s^{-1}$.

The diffusion of larger protein molecules (bovine serum albumin (BSA) with molecular weight 67 kDa) in an NIPAAM-based hydrogel with the thickness between 600 and 700 nm was observed by with coupled LRSP modes.[18] These modes were excited at two distinct angles θ_a and θ_b shown in the reflectivity spectrum in Figure 11(a) and they exhibited penetration depths $L_p^d = 950$ nm (for mode at θ_a) and $L_p^d = 364$ nm (for mode at θ_b). Therefore, the probing by modes at θ_a and θ_b allowed the observation of BSA diffusion in the whole volume of the gel and at close proximity to the gel inner surface, respectively. The kinetics $\theta_a(t)$ and $\theta_b(t)$ were measured after the injection of BSA (at time $t = 0$) and after the surface rinsing ($t = 10$ min) for hydrogel with low cross-linking density (A, polymer volume content $f \sim 8\%$) and large cross-linking density (B, polymer volume content $f \sim 13\%$). The measured data shown in Figure 11(**b**) reveal that the resonances θ_a and θ_s shift toward higher angles upon the diffusion of BSA into a hydrogel due to the increasing of its refractive index n_h. The sensor response approaches equilibrium faster for the hydrogel A than for the hydrogel B, indicating that the diffusion is slower in a denser gel. In addition, for the denser gel B, the initial slope of the sensor response measured after $t = 0$ is larger at θ_a than that at θ_s. The reason for this observation is that the field of coupled LRSP excited at the angle θ_a penetrates deeper into the hydrogel film where BSA molecules diffuse faster from the solution compared to the more confined field generated at θ_b.

Aulasevich *et al.*[53] employed spectroscopy of hydrogel-guided waves for the *in situ* measurement of the concentration of protein molecules (IgG antibody) covalently coupled into a swollen NIPAAM-based hydrogel. This hydrogel carried carboxylic moieties to which IgG molecules were covalently bound by using amine coupling chemistry. Figure 12 shows the reflectivity spectrum for the bare gel (I), spectrum measured after the convertion of carboxylic groups to active ester by using sodium *para*-tetrafluorophenol sulfonate followed by diffusion and reaction of IgG via their amino groups (II), and spectrum after the incubation with ethanolamine and rinsing in order to block the unreacted active esters and expel weakly bound molecules (spectrum III). The spectra exhibit three resonant dips associated with the excitation of two HW modes (noted as TM_1 and TM_2) and SP mode at the interface between gold and hydrogel. The fitting of the spectra I–III revealed that the loading of gel with IgG induced a decrease in the thickness from $d_h = 2.5$–$1.94\,\mu m$ and an increase in the refractive index from $n_h = 1.3467$ to 1.3757. These data correspond to a huge change of surface mass density from $\Gamma = 171\,ng\,mm^{-2}$ to $407\,ng\,mm^{-2}$. After the incubation in ethanolamine, the resonant dips shifted to lower angles as the loosely bound IgG molecules were expelled from the gel (see spectrum III). This leads to a decrease in the gel surface mass density to $190\,ng\,mm^{-2}$ and an increase of the thickness to $d_h = 3.2\,\mu m$. The thickness increase can be attributed to electrostatic repulsion within the gel between bound IgG molecules. The surface mass density of the covalently immobilized IgG molecules of $\Delta\Gamma = 19\,ng\,mm^{-2}$ was determined as the difference between the surface mass density Γ before the gel activation and after the incubation in ethanolamine. These results illustrate that for the investigation of reactions in a

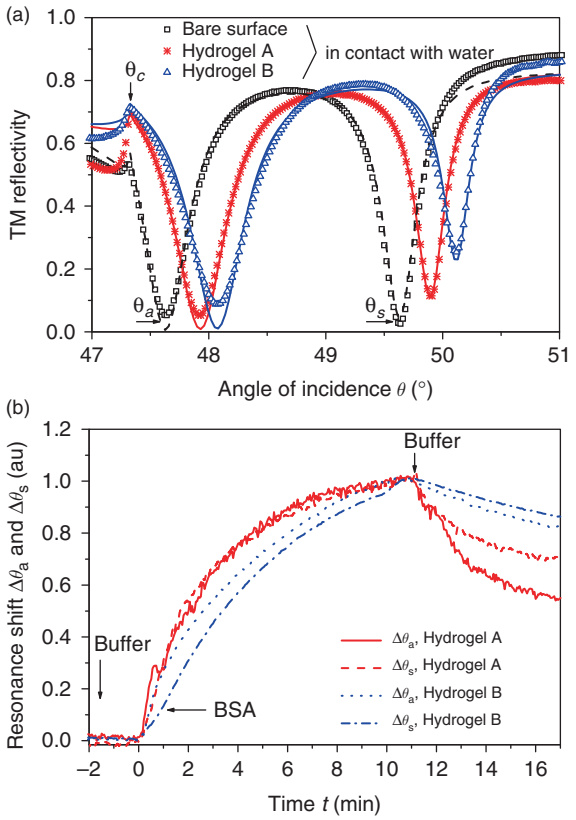

Figure 11 (a) Angular reflectivity spectra measured for the excitation of coupled LRSPs probing an NIPAAM-based hydrogel layer that was cross-linked for 15 min (A, asterisk) and 40 min (B, triangle). (b) Time evolution of sensor signal measured for coupled LRSPs with the penetration depth of $L_p^d = 950$ nm ($\Delta\theta_a$) and $L_p^d = 364$ nm ($\Delta\theta_b$) when BSA molecules diffused through a highly swollen hydrogel (A) and dense hydrogel (B); hydrogel film thickness of $d_h = 600$–700 nm.

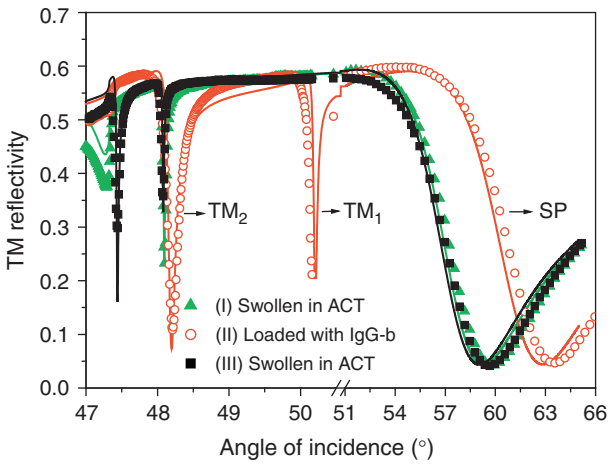

Figure 12 Reflectivity spectra measured for NIPAAM-based hydrogel film that is (I) swollen in acetate buffer, (II) loaded with IgG molecules and (III) after the incubation in ethanolamine incubation.

flexible polymer matrix, both the refractive index and the thickness of the gel need to be determined in order to decouple the changes in the surface mass from those that are related to variations of matrix swelling.

The distribution of protein analyte that was affinity bound in a hydrogel film to immobilized catcher molecules was investigated by using LRSP field-enhanced fluorescence spectroscopy by Huang *et al.*[29] These authors measured kinetics of a fluorescence light intensity emitted from captured chromophore-labeled protein molecules that were excited by the LRSP evanescent field. Figure 13 shows the dependence of the fluorescence signal measured after 30 min flow of a sample on the thickness of the hydrogel film d_h. From data presented in Figure 13(**a**), it follows that after the binding of analyte from a sample with large concentration $\alpha_0 = 1.3\,\mu M$, the measured fluorescence intensity F increases with the hydrogel thickness d_h and reaches a plateau for a thickness larger than the penetration depth of probing LRSP modes of $L_p/2 = 460$ nm. For about 6 orders of magnitude of lower analyte concentration $\alpha_0 = 0.67$ pM, the measured fluorescence signal F is approximately 5 orders of magnitude smaller and its thickness dependence exhibits different behavior (see Figure 13(**b**)). A maximum fluorescence signal F was measured for the hydrogel thickness between $d_h = 130$ and 410 nm and it sharply decreases when increasing the thickness above these values. The sharp decrease in the sensor signal is due to the fact that the majority of the binding sites remain unoccupied upon the incubation with a low concentration of analyte α_0 and thus the binding occurs only within the top slice of the gel with the thickness that is comparable to diffusion penetration depth (see eqn [19]). This depth was estimated as $d_p \sim 400$ nm and, therefore, for thicker hydrogel films the analyte preferably binds at distances at which the excitation LRSP field is weaker leading to a decreasing fluorescence signal (see Figure 9).

2.26.4.4 Interaction Analysis and Detection of Biomolecules

SPR biosensors represent an established technology for biomolecular interaction analysis (BIA).[54,55] In this method, one of the interacting molecules is immobilized on the surface (ligand) and the binding of its affinity partner contained in a solution (analyte) is monitored through binding-induced

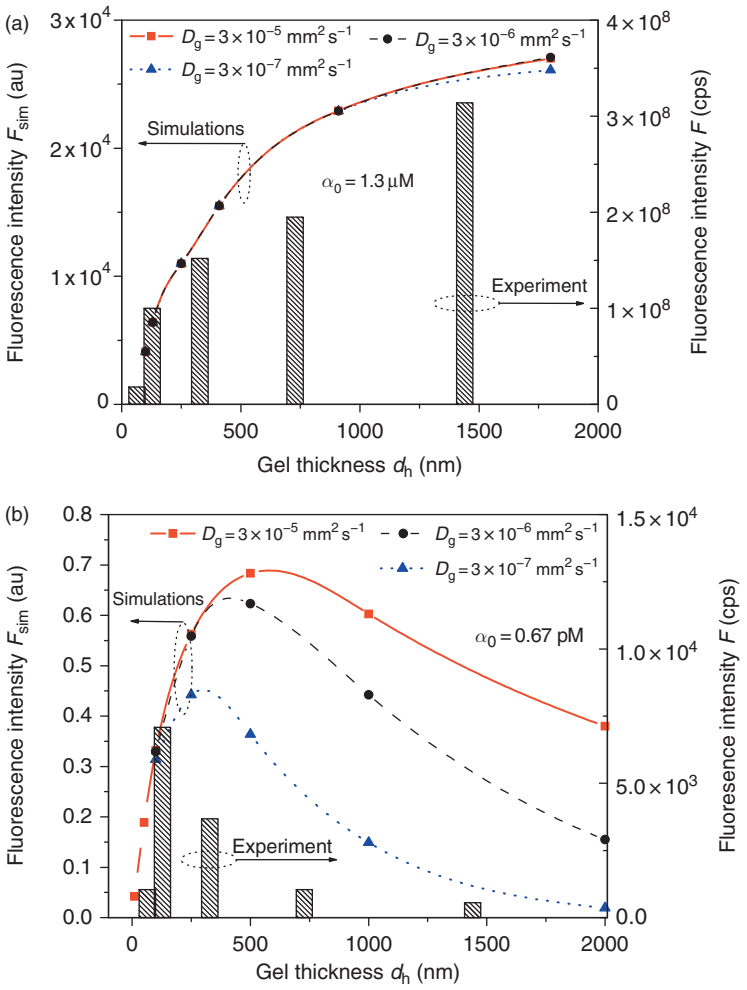

Figure 13 The comparison of simulations (left axis) and measured (right axis) dependence of the fluorescence signal F due to captured chromophore-labeled molecules on the thickness of the hydrogel binding matrix d_h. The hydrogel matrix was probed by LRSP mode. The fluorescence signal after the 30 min flow of a-IgG dissolved at (a) low concentration of $\alpha_0 = 0.67$ pM and (b) high concentration of $\alpha_0 = 1.3\,\mu M$ is presented. Diffusion coefficient in the gel of $D_g = 3 \times 10^{-5}$ mm^2 s^{-1} (black ■), $D_g = 3 \times 10^{-6}$ mm^2 s^{-1} (red ●), and $D_g = 3 \times 10^{-7}$ mm^2 s^{-1} (blue ▲) was assumed.

refractive index changes. Polymer binding matrices based on carboxylated dextran brushes represent widely used surface architecture for the immobilization of ligands in SPR sensor technology.[56] In general, highly open 3D polymer matrices with flexible polymer chains can accommodate larger amounts of ligands and provide better accessibility for molecular binding with lower steric hindrance compared to 2D architectures based on, for example, self-assembled monolayers.

For the biomolecular interaction analysis, kinetics of the SPR sensor response for the association phase is first measured. In this phase, the sensor signal gradually increases with time due to the capture of analyte from a sample on the surface. Afterward, the dissociation phase is recorded in which the sensor surface is rinsed with a buffer without the analyte leading to a gradual decrease of the sensor response due to the release of captured analyte (see **Figure 14** from Wang *et al.*[58]). By fitting the association and dissociation phase of the kinetics with a model, the affinity binding rate constants k_a and k_d can be determined. For many cases, the model introduced in Section 2.26.3.3 can be adopted in a simplified form. First, the experiment can be designed so the diffusion mass transfer k_m is much faster than the affinity binding rate $k_a\beta$ at the surface. This can be achieved by, for example, using a low concentration of the catcher molecules β. Second, polymer matrices with small thickness $d_h \sim 100$ nm and large swelling ratio are typically used. For such systems, the concentration of captured molecules γ is constant through the gel and the binding kinetics depends weakly on the diffusion of analyte through the polymer matrix. With these approximations, the SPR sensor response kinetics can be fitted with the solution of eqn [13] that can be found analytically. More detailed information and a variety of models can be found in numerous excellent reviews or books.[23]

Another important application area of SPR biosensors is rapid detection of chemical and biological analytes related to important fields such as medical diagnostics (e.g., biomarkers and hormones), food control (e.g., pathogens and toxins), or environmental monitoring (e.g., pollutants).[10] In these applications, analysis of real samples such as blood plasma or food-derived matrices remains a challenge due to the nonspecific interaction with the functionalized sensor surface that leads to a false response. Recently, intensive research in new polymer materials with antifouling properties has been carried out.[57] In this field, SPR method provides convenient and sensitive means for the characterization of such surfaces.

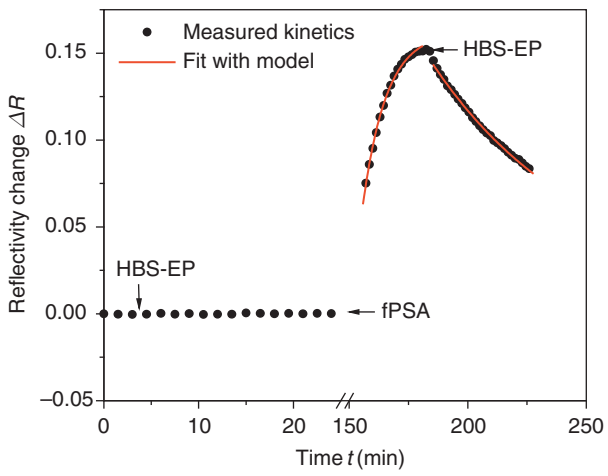

Figure 14 Time evolution of SPR signal upon the capture (association phase) and release of target analyte (dissociation phase) from a hydrogel film with immobilized ligand molecules. Binding of prostate specific antigen to respective antibodies coupled in a dextran-based hydrogel that is probed with an LRSP mode is presented.

2.26.5 Conclusion

Spectroscopy of SP and polymer waveguide modes allows the observation of a wide range of important characteristics of thin polymer films. These methods can be implemented by using numerous SPR instruments that become commercially available and provide a convenient means for the design of functional polymer architectures to serve in applications such as antifouling coatings, responsive materials for drug delivery, antimicrobial surfaces, and biointerfaces for detection of molecular and biological analytes. The future research will be particularly focused on improving the sensitivity and implementation of schemes for high-throughput observation of polymer interactions. In addition, combining with other methods, such as quartz crystal microbalance (QCM), electrochemistry and fluorescence spectroscopy, can greatly extend the potential of this platform and provide more detailed information on studied polymer assemblies.

Acknowledgements

Support for this work was provided in part by the Center of Innovation and Technology of Vienna (ZIT) and Austrian NANO Initiative (FFG and BMVIT) through the NILPlasmonics project within the NILAustria cluster (www.NILAustria.at).

References

1. Ekblad, T.; Bergstroem, G.; Ederth, T.; *et al. Biomacromolecules* **2008**, *9*, 2775–2783.
2. Xu, F.; Persson, B.; Lofas, S.; Knoll, W. *Langmuir* **2006**, *22*, 3352–3357.
3. Jacobsen, V.; Menges, B.; Forch, R.; *et al. Thin Solid Films* **2002**, *409*, 185–193.
4. Plum, M. A.; Steffen, W.; Fytas, G.; *et al. Opt. Express* **2009**, *17*, 10364–10371.
5. Gianneli, M.; Beines, P. W.; Roskamp, R. F.; *et al. J. Phys. Chem. C* **2007**, *111*, 13205–13211.
6. Knoll, W. *Annu. Rev. Phys. Chem.* **1998**, *49*, 569–638.
7. Barbey, R.; Lavanant, L.; Paripovic, D.; *et al. Chem. Rev.* **2009**, *109*, 5437–5527.
8. Berggard, T.; Linse, S.; James, P. *Proteomics* **2007**, *7*, 2833–2842.
9. Hook, A. L.; Thissen, H.; Voelcker, N. H. *Langmuir* **2009**, *25*, 9173–9181.
10. Homola, J. *Chem. Rev.* **2008**, *108*, 462–493.
11. Blondelle, S. E.; Lohner, K.; Aguilar, M. I. *Biochim. Biophys. Acta-Biomembr.* **1999**, *1462*, 89–108.
12. Arima, Y.; Iwata, H. *Biomaterials* **2007**, *28*, 3074–3082.
13. Katsamba, P.; Carroll, K.; Ahlsena, G.; *et al. Proc. Natl. Acad. Sci. U.S.A* **2009**, *106*, 11594–11599.
14. Byrne, M. E.; Salian, V. *Int. J. Pharm.* **2008**, *364*, 188–212.
15. Rather, H. *Surface Plasmons on Smooth and Rough Surfaces and on Gratings*; Springer-Verlag: Berlin, **1983**.
16. Sarid, D. *Phys. Rev. Lett.* **1981**, *47*, 1927–1930.
17. Dostalek, J.; Kasry, A.; Knoll, W. *Plasmonics* **2007***b*, *2*, 97–106.
18. Dostalek, J.; Roskamp, R. F.; Knoll, W. *Sens. Actuators B Chem.* **2009**, *139*, 9–12.

19. Nenninger, G. G.; Tobiska, P.; Homola, J.; Yee, S. S. *Sens. Actuators B Chem.* **2001**, *74*, 145–151.
20. Wark, A. W.; Lee, H. J.; Corn, R. M. *Anal. Chem.* **2005**, *77*, 3904–3907.
21. Vala, M.; Dostalek, J.; Homola, J. *SPIE* **2007**, *6585*, 658522–658521.
22. Huang, C. J.; Dostalek, J.; Knoll, W. *J. Vac. Sci. Technol. B* **2010***b, 28*, 66–72.
23. Homola, J. *Surface Plasmon Resonance (SPR) Sensors*; Springer: New York, **2006**.
24. Laschitsch, A.; Menges, B.; Johannsmann, D. *Appl. Phys. Lett.* **2000**, *77*, 2252–2254.
25. Schlereth, D. D.; Kooyman, R. P. H. *J. Electroanal. Chem.* **1998**, *444*, 231–240.
26. Dostalek, J.; Knoll, W. *Biointerphases* **2008**, *3*, 12–22.
27. Junk, M. J. N.; Anac, I.; Menges, B.; Jonas, U. *Langmuir* **2010**, *16*, 12253–12259.
28. Yeh, P. *Optical Waves in Layerd Media*; Wiley: New York, 1988; pp 102–114.
29. Huang, C. J.; Dostalek, J.; Knoll, W. *Biosens. Bioelectron.* **2010**a, doi: 10.1016/j.bios.2010.07.072.
30. Beines, P. W.; Klosterkamp, I.; Menges, B.; *et al. Langmuir* **2007**, *23*, 2231–2238.
31. Pincenti, J. C.; Goel, S.; Naylor, D. L. *Appl. Opt.* **1993**, *32*, 322–326.
32. Koynov, K.; Bahtiar, A.; Ahn, T.; *et al. Macromolecules* **2006**, *39*, 8692–8698.
33. Born, M.; Wolf, E. *Principles of optics*; Pergamon: London, **1980**.
34. Granqvist, C. G.; Hunderi, O. *Phys. Rev. B* **1977**, *16*, 3513.
35. Liedberg, B.; Lundstrom, I.; Stenberg, E. *Sens. Actuators B Chem.* **1993**, *11*, 63–72.
36. Wang, Y.; Huang, C. J.; Jonas, U.; *et al. Biosens. Bioelectron.* **2010**, *25*, 1663–1668.
37. Milner, S. T. *Macromolecules* **1991**, *24*, 3704–3705.
38. Edwards, D. A. *Bull. Math. Biol.* **2001**, *63*, 301–327.
39. Jossang, T.; Feder, J.; Rosenqvist, E. *J. Protien Chem.* **1988**, *7*, 1573–4943.
40. Schuck, P. *Biophys. J.* **1996**, *70*, 1230–1249.
41. Sikavitsas, V.; Nitsche, J. M.; Mountziaris, T. J. *Biotechnol. Prog.* **2002**, *18*, 885–897.
42. Brandani, P.; Stroeve, P. *Macromolecules* **2003**, *36*, 9502–9509.
43. Plunkett, M. A.; Wang, Z. H.; Rutland, M. W.; Johannsmann, D. *Langmuir* **2003**, *19*, 6837–6844.
44. Munakata, H.; Takagaki, K.; Majima, M.; Endo, M. *Glycobiology* **1999**, *9*, 1023–1027.
45. Nestle, N. F. E. I.; Kimmich, R. *J. Phys. Chem.* **1996**, *100*, 12569–12573.
46. Harmon, M. E.; Jakob, T. A. M.; Knoll, W.; Frank, C. W. *Macromolecules* **2002**, *35*, 5999–6004.
47. Kuckling, D.; Harmon, M. E.; Frank, C. W. *Macromolecules* **2002**, *35*, 6377–6383.
48. Sorrell, C. D.; Lyon, L. A. *J. Phys. Chem. B* **2007**, *111*, 4060–4066.
49. van den Brom, C. R.; Brunsen, A.; Roskamp, R. F.; Jonas, U. In *Handbook of Biofunctional Surfaces*; Knoll, W., Ed.; Pan Stanford Publishing: Singapore, 2010.
50. Adam, P.; Dostalek, J.; Homola, J. *Sens. Actuators B Chem.* **2006**, *113*, 774–781.
51. Dostalek, J.; Adam, P.; Kvasnicka, P.; *et al. Opt. Lett.* **2007***a, 32*, 2903–2905.
52. Podgorsek, R. P.; Franke, H. *Appl. Phys. Lett.* **1998**, *73*, 2887–2889.
53. Aulasevich, A.; Roskamp, R. F.; Jonas, U.; *et al. Macromol. Rapid Comm.* **2009**, *30*, 872–877.
54. De Crescenzo, G.; Boucher, C.; Durocher, Y.; Jolicoeur, M. *Cell. Mol. Bioeng.* **2008**, *1*, 204–215.
55. Richter, A.; Paschew, G.; Klatt, S.; *et al. Sensors* **2008**, *8*, 561–581.
56. Lofas, S.; Malmqvist, M.; Ronnberg, I.; *et al. Sens. Actuators B Chem.* **1991**, *5*, 79–84.
57. Jiang, S. Y.; Cao, Z. Q. *Adv. Mater.* **2010**, *22*, 920–932.
58. Wang, Y.; Brunsen, A.; Jonas, U.; *et al. Anal. Chem.* **2009**, *81*, 9625–9632.

Biographical Sketches

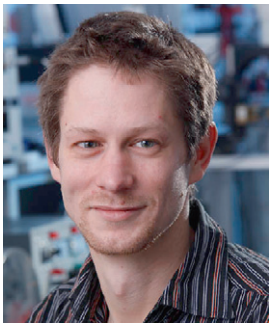

Jakub Dostálek received his PhD from the Charles University and was Faculty of Mathematics and Physics in Prague (Czech Republic) in 2006. From 2000 to 2006, he worked as a research assistant at the Institute of Photonics and Electronics in Prague (Czech Republic). From 2006 to 2007, he was a postdoctoral fellow at the Max-Planck Institute for Polymer Research in Mainz (Germany) and during 2007–2008 he worked there as a project leader in the Department of Materials Research. Since 2009, he has held a project manager position at the Austrian Institute of Technology in Vienna (Austria). His research interests include nanomaterials, plasmonics, plasmon-enhanced fluorescence, and hydrogel biointerfaces applied in biosensors for medical diagnostics and food control. Dostálek has authored 6 book chapters and around 25 papers in peer review scientific journals that have received around 500 citations.

Wolfgang Knoll has been a managing director of AIT since 2008. He holds a professor position in the Department of Nanobiotechnology at the University of Natural Resources and Applied Life Sciences (BOKU). In addition, he is Visiting Principal Scientist at the Institute of Materials Research and Engineering (IMRE), Singapore, and Adjunct Professor at Hanyang University, Korea. Knoll's research interests embrace materials sciences. He has authored more than 700 papers in peer review scientific journals that have received more than 15 000 citations.